



Transient Unidirectional Solidification, Microstructure and Intermetallics in Sn-Ni Alloys[†]

Clarissa Barros da Cruz^a, Rafael Kakitani^a, Marcella Gautê Cavalcante Xavier^b, Bismarck Luiz Silva^a ,
Amauri Garcia^a, Noé Cheung^a, José Eduardo Spinelli^b 

^aDepartamento de Engenharia de Materiais e Manufatura, Universidade de Campinas - UNICAMP, 13083-860, Campinas, SP, Brasil

^bDepartamento de Engenharia de Materiais, Universidade Federal de São Carlos - UFSCar, 13565-905, São Carlos, SP, Brasil

^cDepartamento de Engenharia de Materiais, Universidade Federal do Rio Grande do Norte - UFRN, 59078-970, Natal, RN, Brasil

Received: December 16, 2017; Revised: February 23, 2018; Accepted: February 28, 2018

The present research work examines the microstructural arrangements formed during the transient solidification of eutectic Sn-0.2wt.%Ni and hypereutectic Sn-0.5wt.%Ni alloys. Also, it examines their respective correlations with solidification thermal parameters: eutectic growth rate (V_E) and eutectic cooling rate (\dot{T}_E); length scales of matrix and eutectic phases: microstructural spacings and the corresponding tensile properties: ductility and strength. Both alloys were directionally solidified upwards under unsteady-state regime, and characterized by optical and scanning electron microscopy. Concerning the hypereutectic Sn-0.5wt.%Ni, the increase in Ni content is shown to influence both thermal behavior and cellular spacing (λ_c). The NiSn₄ intermetallics is present in the eutectic mixture of both alloys, whilst in the Sn-0.5wt.%Ni alloy the primary phase has been identified by SEM-EDS as the Ni₃Sn₄ intermetallics. A β -Sn morphological cellular/dendritic transition occurs in the 0.2wt.%Ni eutectic alloy for $\dot{T}_E > 1.2\text{K/s}$. Despite that, regular cells in the hypereutectic alloy (0.5wt.%Ni) turns into plate-like cells for $\dot{T}_E > 1.4\text{K/s}$. If considered a reference cellular spacing about $20\mu\text{m}$ (i.e., $\lambda_c^{-1/2}=0.22$), the samples associated with the Sn-0.5wt.%Ni alloy are shown to be associated with higher tensile strengths, but much lower ductility as compared with the corresponding results of the eutectic alloy.

Keywords: Lead-free alloys, Transient solidification, Microstructure, Intermetallics, Tensile properties, Wettability.

1. Introduction

Nickel (Ni) is one of the main alloying elements of Sn-based lead-free solder alloys. It has been largely added as third or as fourth element in Sn-Ag or Sn-Ag-Cu alloys, respectively. It is worth noting that the additions of minor alloying elements to Sn-based lead-free solders has received a lot of attention recently in order to boost or fine-tune various application properties¹⁻⁶. For example, Wang *et al.*⁷ found that Ni concentrations higher than 0.01 wt.% added to a Sn-2.5Ag-0.8Cu alloy may retard the growth of deleterious Cu₃Sn particles layers at the alloy/copper interface even after an aging time of 2000 h. According to Nishikawa *et al.*⁸ the addition of 0.1 wt.% Ni to a Sn-3.5Ag alloy does not affect the joint mechanical strength with a Cu pad, but it changes the fracture mode.

The sustainable development of soldering processes experiences a change towards lead-free electronic products, the so called green electronics^{9,10}. Consequently, manufacturers are required to set their furnaces and

procedures for the application of lead-free solder alloys. This is explained by the recent legal restrictions put in place for lead-based solders. Sn-Ni alloys are considered possible substitutes, even though there is a lack of studies devoted to their microstructures and application properties^{11,12}.

Understanding the microstructure evolution in these alloys as well as establishing correlations between microstructural features and solidification thermal parameters (i.e., cooling rate and solidification velocity) is fundamental for the pre-programming of final application properties of as-soldered joints. Determination of solidification conditions might yield either a specified β -Sn morphology and size or a required intermetallic particle in eutectic and hypereutectic Sn-Ni alloys.

Such lack of knowledge regarding Sn-Ni alloys is quite unexpected considering that Ni is a very common substrate in electronic packaging. Ni is largely employed since soft soldering applications involving Ni and Sn represent slower growth kinetics as compared, for example, with that occurring between Cu and Sn¹². The existing research efforts dedicated to Sn-Ni solder alloys put emphasis on examining and identifying the formed intermetallics in compositions of interest. One of the few

*e-mail: spinelli@ufscar.br

[†]Article presented in the ABM Week 2017, October 2nd to 6th, 2017, São Paulo, SP, Brazil

studies has shown that the NiSn_4 intermetallics (IMC) can be formed by either primary precipitation during solidification or eutectic transformation¹¹⁻¹³. Overall, the Sn-Ni Sn_4 eutectic structure has been identified as the predominant one regardless the tested solidification conditions, which varied from 120K/s to 0.022K/s¹¹. The same research showed that for hypereutectic compositions and solidification cooling rates in the range 1-10K/s, a very large fraction of primary Ni_3Sn_4 IMC grew to the detriment of the primary NiSn_4 IMC.

Various studies devoting to develop alternative and new solder alloys have been recently performed¹⁴⁻²⁰. The aim was to characterize microstructure features and determine their correlations with solidification thermal parameters, that is, the eutectic growth rate (V_E) and the eutectic cooling rate (\dot{T}_E). This kind of knowledge ought to be expanded for Sn-Ni alloys. Within this approach, the main priority is to compare the final microstructures and how they could be induced via solidification cooling rate. In addition, in what manner the Ni content can affect the microstructure features and properties such as wettability and tensile properties. In general, the soundness of an alloy depends on the morphology/size of the β -Sn matrix and on the size/nature of phases surrounding it^{21,22}.

The microstructure features of directionally solidified Sn-0.7Cu alloys containing minute additions of Ni were recently investigated. It has been reported that Ni modified alloys with 500 ppm and 1000 ppm of Ni developed both the $(\text{Cu,Ni})_6\text{Sn}_5$ phase and the Ni_3Sn_4 primary IMC for specimens experiencing fast cooling conditions²³. Within this work, the mean equilibrium contact angles determined for the Sn-0.7Cu, Sn-0.7Cu-0.05Ni and Sn-0.7Cu-0.1wt%Ni alloys were 19.1°, 12.9° and 36.0° respectively. These values can be considered compatible to those reported for Sn-Pb alloys.

According to Kong *et al.*²⁴, the increase in Sn content of Sn-Ni alloys can lead to better wettability, and such alloys are often required in practical applications mainly because of such essential quality.

In order to gain insight into microstructure formation and solidification thermal parameters of eutectic Sn-0.2wt.%Ni and hypereutectic Sn-0.5wt.%Ni solder alloys, the present study aims to examine the experimental growth dependence of microstructure features on the solidification cooling rate- \dot{T} . Furthermore, the formation of intermetallics (either primary or eutectic) and the morphology and scale of the β -Sn phase will be discussed with basis on the cooling rate and alloy Ni content. The cooling conditions provided in the present experiments are expected to permit the formation of some metastable intermetallic phases. This way, the morphologies of stable and/or metastable eutectics will be assessed. Correlations

between tensile strength, ductility and representative length scale of the microstructure are investigated.

2. Experimental Procedure

2.1. Directionally solidified castings

The eutectic Sn-0.2 wt. %Ni and the hypereutectic Sn-0.5 wt. %Ni alloys have been assessed. Within this purpose, two directionally solidified (DS) Sn-Ni alloys castings were produced by using a water-cooled setup as shown in Fig. 1²⁵. The referred solidification system gives rise to unsteady-state solidification conditions. The surface of the AISI 1020 low carbon steel bottom-part mold has been finished with a 1200 grit SiC abrasive paper. The following procedures were performed for each alloy: firstly, the alloy is melted *in situ* by radial electrical wiring positioned around a cylindrical stainless-steel container. Secondly, when the melt temperature is about 10% above either the eutectic (0.2Ni) or the *liquidus* (0.5Ni) temperatures, the electric heaters are disconnected and at the same time the water flow at the bottom of the container is started, which allows the onset of solidification. Finally, the evolution of temperatures along the length of the castings was monitored by fine type J thermocouples (0.2 mm diameter wire), placed in the geometrical center of the cylindrical mold cavity along its length. A detail of the thermocouples position can be seen in the bottom (right corner) of Fig. 1.

These cooling curves have been used to generate the values of eutectic (\dot{T}_E) and tip (\dot{T}_L) cooling rates and of eutectic (V_E) and tip (V_L) growth rates for both alloys. The method allows plot the growth rates of various relative positions (P) along the length of the casting^{5,6}. It is based on tracking the passage of the solidification front (liquidus or eutectic isotherms) by each thermocouple in order to relate the thermocouple tracked position (P) with the corresponding time (either t_E or t_L). Then, this procedure is replicated for various positions.

The eutectic and tip cooling rates were determined by considering the thermal data recorded immediately after the passage of the eutectic and *liquidus* fronts respectively by each thermocouple. Both eutectic and *liquidus* fronts were considered in the case of the hypereutectic Sn-0.5wt.%Ni alloy while only the eutectic front was followed for the eutectic Sn-0.2wt.%Ni alloy. The eutectic thermal parameters (\dot{T}_E and V_E) for both alloys were those finally considered for comparison purposes. Consequently, the effects of the alloy Ni content on the solidification kinetics could be assessed.

There are various ways to define the cooling rate during a solidification process. One can either follow the slope of the cooling curve at a certain temperature or divide the solidification temperature interval (liquidus minus solidus) by the time required to complete solidification. In the present manuscript we have experimentally determined both variations in tip and eutectic cooling rates for both Sn-Ni

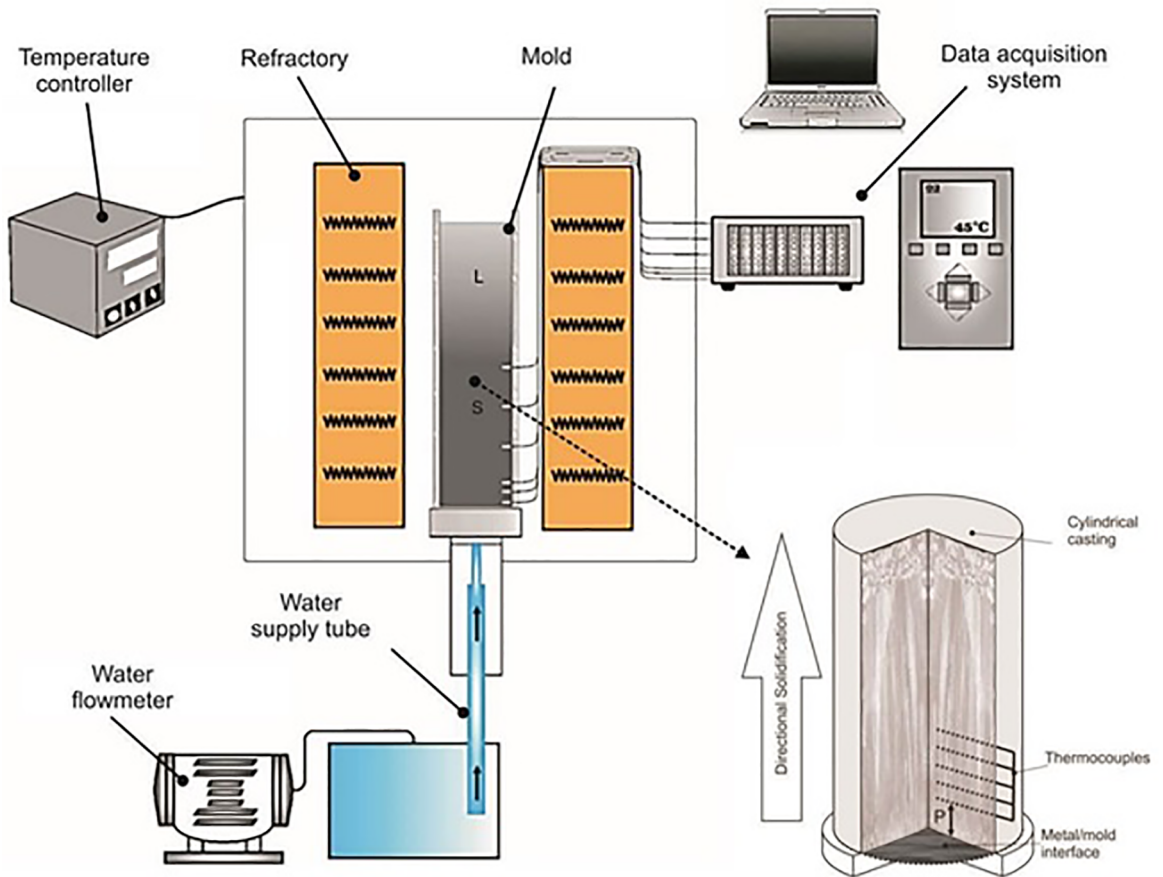


Figure 1. Vertical upward directional solidification casting assembly and connected devices used to produce the directionally solidified Sn-Ni alloys castings

alloys. This means that the slopes of the cooling curves were determined taking as references the characteristic liquidus and eutectic temperatures of the examined alloys.

2.2. Metallography, tensile and wetting tests

Metallographic analysis was performed to reveal the microstructural and morphological details of both Sn-Ni alloys castings, using grinding and polishing steps combined with the etchant: 95 mL of H₂O, 2.5 mL of HNO₃, 1.5 mL of HCl and 1.0 mL of HF.

Micrographs were obtained using a light microscope with a coupled optical image processing system Olympus, BX41M-LED (Olympus Co., Japan) and using a Field Emission Gun (FEG) - Scanning Electron Microscope SEM-EDS FEI (Inspect S50L). The triangle method was employed to determine the cellular spacing (λ_c) on transverse sections of the DS castings^{26,27}.

Transverse specimens extracted from different positions along the length of the DS castings were prepared according to specifications of the ASTM Standard E 8M/04 and tested in an Instron 5500R machine at a strain rate of about $1 \times 10^{-3} \text{ s}^{-1}$. The ultimate tensile strength and strain-to-failure have been determined and related to average microstructural spacings.

A goniometer Krüss DSHAT HTM Reetz GmbH model allowed the measurement of contact angles (θ) for each solder alloy/carbon steel substrate²². The data of the tests were all acquired in triplicate.

3. Results and Discussions

3.1. Solidification thermal parameters

Temperatures recorded during solidification of the Sn-Ni alloys allowed the plots in Fig. 2 to be generated. A severe temperature reduction over time can be observed for positions very close to the cooled bottom of the DS castings (i.e, black and red lines+symbols). This fast cooling is explained because these positions are those closer to the water-cooled surface of the mold, where heat extraction is very efficient. The moderate cooling associated with the subsequent positions higher than ~10mm is due to presence of both an already solidified layer and a gap formed between metal and mold caused by volumetric shrinkage accompanying solidification.

The cooling curves of Fig. 2 were used to generate plots of position (P), from the metal/mold interface,

with the corresponding times (t_E , t_L) of the eutectic and liquidus fronts passing by each thermocouple, i.e., $P=f(t_E)$ and $P=f(t_L)$. As a result, experimental fitting functions

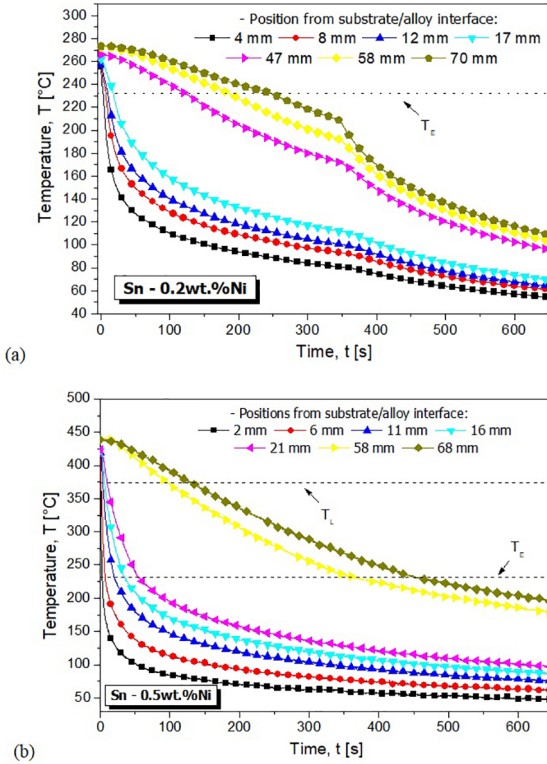


Figure 2. Thermal profiles generated through transient directional solidification of: (a) Sn-0.2wt.%Ni and (b) Sn-0.5wt.%Ni alloys DS castings. T_L is liquidus temperature and T_E is eutectic temperature as pointed out inside the graphs

were obtained. Time-derivative of these functions were carried out so that the eutectic growth rate (V_E) and the tip growth rate (V_L) could be calculated in the forms of $V=f(t_E)$ and $V=f(t_L)$. By replacing $t=f(P)$ with t inside the equation for V , resultant equations of the forms $V_E=f(P)$ and $V_L=f(P)$ have been obtained.

The experimental evolution of cooling rates (\dot{T}) and growth rates (V) along the length of both Sn-0.2 and 0.5wt.%Ni alloys castings are plotted in Fig. 3 and Fig. 4, respectively. These solidification thermal parameters were charted against the position P in the castings, so that the influence of the alloy Ni content could be noticed. Within these graphs, the first noted feature is that both tip cooling (\dot{T}_L) and growth (V_L) rates profiles for the Sn-0.5wt.%Ni alloy casting are much higher than the eutectic referred values \dot{T}_E and V_E . This difference is more substantial for positions (P) closer to the bottom of the casting.

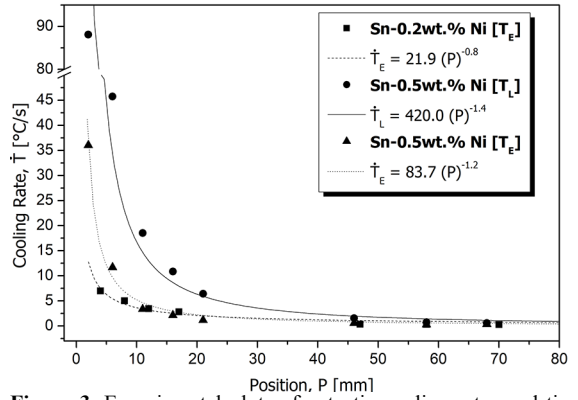


Figure 3. Experimental plots of eutectic cooling rates and tip cooling rates for: Sn-0.2 and 0.5 wt.%Ni alloys along the length of the directionally solidified castings

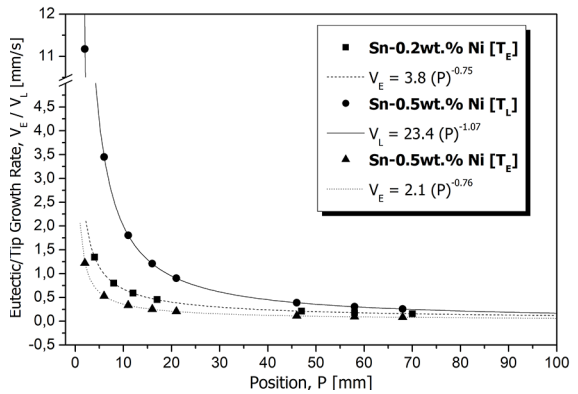


Figure 4. Experimental plots of eutectic growth rates and tip growth rates for: Sn-0.2 and 0.5 wt.%Ni alloys along the length of the directionally solidified castings

The eutectic-related profiles in Fig. 3 and Fig. 4 (triangles and squares) depict higher cooling rates for the hypereutectic alloy whilst very close V_E values can be observed when the Sn-0.2 and 0.5wt.%Ni alloys are compared. From $P=10$ mm onwards both alloys present very similar experimental evolutions of both \dot{T}_E and V_E .

3.2. Growth of regular, plate-like cells and dendrites

Vertically aligned columnar grains formed the macrostructures revealed for the DS Sn-0.2wt.%Ni and Sn-0.5wt.%Ni alloys castings, as can be observed in the central images of Fig. 5 and Fig. 6. The grains follow the direction of growth, which is mainly parallel to the heat flow pathways as projected downwards. Large primary intermetallics can be observed in the microstructures of the Sn-0.5wt.%Ni alloy in Fig. 6. The equilibrium microstructures of hypereutectic Sn-Ni alloys consist of primary Ni_3Sn_4 crystals enveloped in a β -Sn+ Ni_3Sn_4 eutectic mixture¹¹, while for the eutectic

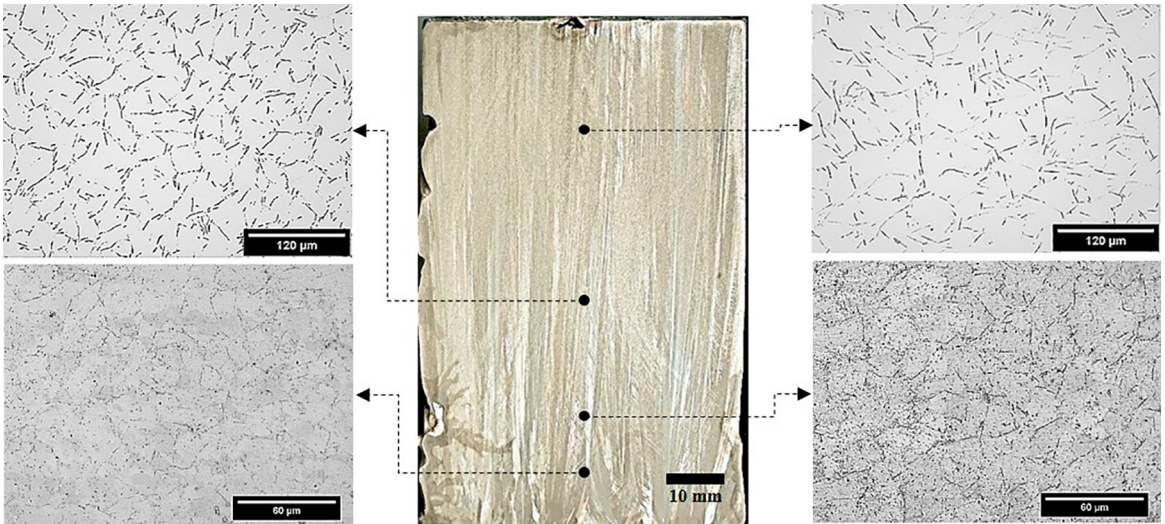


Figure 5. Columnar grains macrostructure and selected transverse microstructures showing the β -Sn morphological evolution across the Sn-0.2wt.%Ni alloy casting

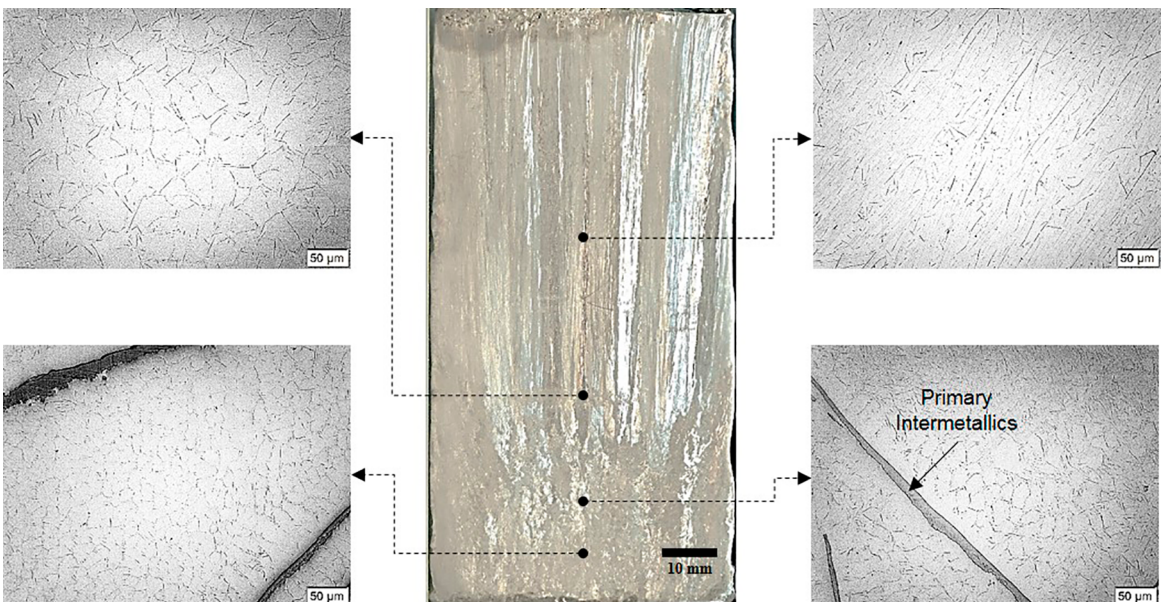


Figure 6. Columnar grains macrostructure and selected transverse microstructures showing the β -Sn morphological evolution from the bottom to top of the Sn-0.5wt.%Ni alloy casting

Sn-Ni alloy the equilibrium microstructure is formed by the β -Sn+Ni₃Sn₄ mixture. However, the growth of β -Sn cells and intermetallic particles appears to prevail in all Sn-Ni alloys samples, despite the presence of primary intermetallics for the Sn-0.5wt.%Ni alloy.

It appears that the large primary intermetallics that form first are able to incorporate part of the nickel available in the liquid immediately ahead of the solidification front. Hence, the liquid will become depleted of Ni until it reaches the eutectic composition. Then, one can consider the remaining liquid composition as eutectic (\sim 0.2wt.%Ni) or close to that. It is very hard to distinguish between primary Sn growth and eutectic growth in Sn-Ni alloys

under non-equilibrium conditions because the melting temperature of Sn is 231.96 °C, which is very close to the eutectic temperature of 231.15 °C²⁸. It is worth noting that the displacement of the eutectic isotherm was that considered in the present investigation to determine V_E and \dot{T}_E , as shown in Fig. 3 and Fig. 4. Considering that the present experiments are monitoring macroscopic heat flow conditions during solidification allied to the proximity of the aforementioned transformation temperatures, the eutectic isotherm appears to be the representative of the prevalent growth of β -Sn cells and intermetallic particles in both examined alloys.

Furthermore, the growth of primary phases in the Sn-0.5wt.%Ni alloy may be associated with the V_L and \dot{T}_L .

The occurrence of β -Sn single-phase instabilities during off-eutectic growth of the eutectic phase is due to the long-range boundary layer built up ahead of the solid/liquid interface. Under such conditions, one phase becomes heavily constitutionally undercooled. This can be appreciated from the fact that, in an off-eutectic composition, the alloy *liquidus* temperature is always higher than the eutectic one, as is the case for the Sn-Ni alloys. Consequently, the corresponding primary phase will be more highly undercooled and tend to grow faster than the eutectic²⁹.

As can be seen in Fig. 5 for the Sn-0.2wt.%Ni alloy, a reverse transition from dendrites to cells can be observed for positions, P, higher than 50mm. Within this occurrence, both cells and dendrites come into coexistence for $\dot{T}_E < 1.2$ K/s. This is rather unusual since the regular morphological transition is reported to evolve from cells to dendrites with the increase in cooling rate^{21,29}, which is the opposite of what is observed here.

A recent study on rapid solidification of the Sn-0.7 wt.% Cu by impulse atomization³⁰ stated a prevalence of high-cooling rates cells for cooling rates higher than 12.0 K/s, which is around 10 times higher than the critical value found for the Sn-0.2 wt.% Ni alloy in the present investigation. Moderate values of both growth rate ($V_L > 0.4$ mm/s) and cooling rate ($\dot{T} > 1.2$ K/s) characterized the critical values for the incidence of the so-called high-velocity cells for a Sn- 5.5 wt%Sb alloy. In this case, the critical value for cooling rate is the same as we found in the present study.

Another investigation with the Sn-0.2wt.%Ni alloy against a copper cooled mold induced the occurrence of high cooling rates cells for $\dot{T}_E > 5.5$ K/s, followed by the growth of dendrites with the decrease in the cooling rate. The anticipated growth of dendrites links with cooling rates 4.5 times higher. This appears to be associated with the strong instabilities on the solid/liquid interface motivated by the dissolution of copper from the mold into the liquid. Indeed, copper substrates exhibit higher ability to be dissolved by Sn-based alloys than that offered by steels molds³¹.

As can be seen in the top right corner of Fig. 6, farther away from the bottom surface of the Sn-0.5wt.%Ni alloy, the microstructure is consisted of side by side β -Sn plates. Despite the non-equilibrium solidification conditions, lower cooling rates (<1.4 K/s) seem to induce a plate-like cellular structure to be formed. This finding is in agreement with the reports in the literature. Xu *et al.*³² stated that the growth of cells might follow the path: poxes, plate-like cells and regular cells.

Fig. 7 and Fig. 8 show the experimental variations found for cellular spacing, λ_c , as a function of the eutectic cooling rate and the eutectic growth rate, respectively. Points are average spacing values along with their standard deviations for each position monitored in the DS castings. The exponent -0.55

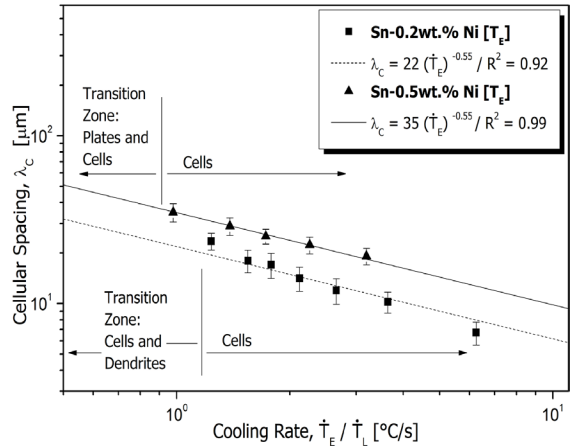


Figure 7. Experimental growth correlations expressing the variation of cellular spacing with the eutectic cooling rate for the Sn-Ni alloys. R^2 is the coefficient of determination

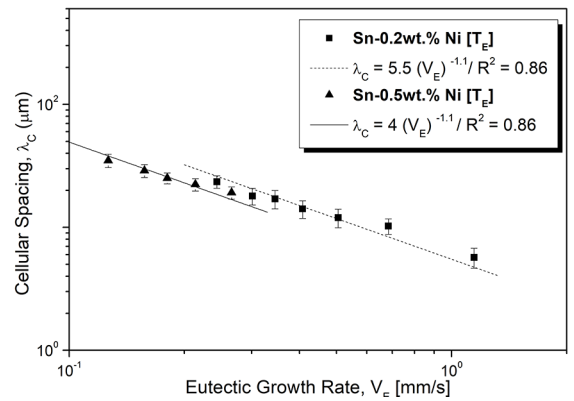
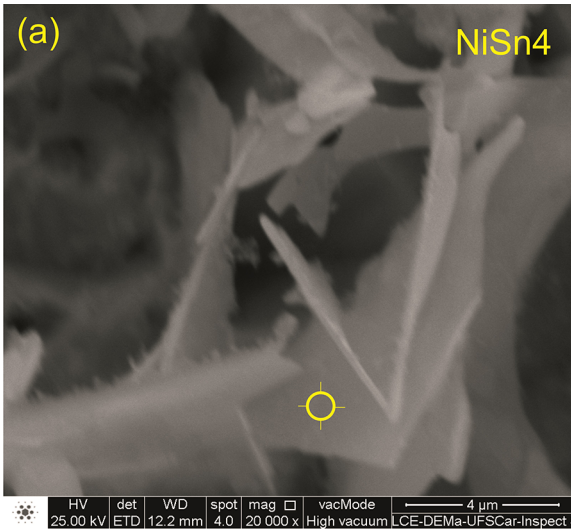


Figure 8. Experimental evolution of cellular spacing with the eutectic growth rate for the Sn-Ni alloys. R^2 is the coefficient of determination

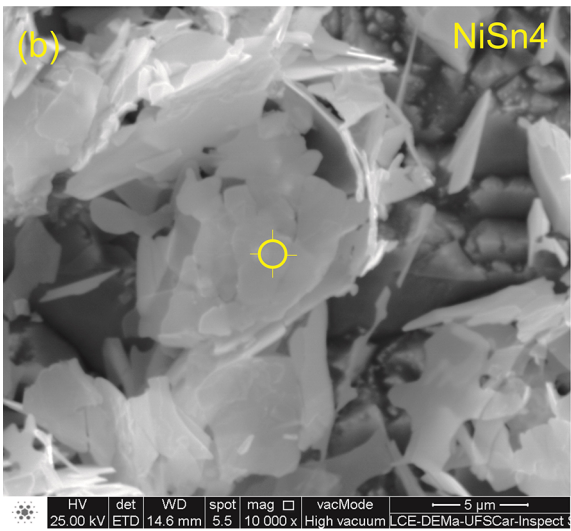
characterizing the cooling rate-dependent power functions is the same reported in other investigations with binary alloys^{6,12,15,17}. When comparing the results for both Sn-Ni alloys, it is possible to infer that, for any considered cooling rate, λ_c of the Sn-0.5wt.%Ni alloy will be higher than that of the Sn-0.2wt.%Ni alloy. However, if a certain growth rate, V_{E^*} is taken in account in Fig. 8 (that is: ~ 0.3 mm/s), very similar microstructural spacings may characterize the length scales of the β -Sn phase related to the Sn-0.2 and 0.5 wt.%Ni alloys.

3.3. Growth of intermetallics (IMC) during transient solidification of Sn-Ni alloys

As previously shown in Fig. 5 and Fig. 6, the intermetallic particles form the boundaries of the β -Sn cells. The SEM-EDS results in Fig. 9 elucidate that the plate-like particles are the non-equilibrium Ni_3Sn_4 IMC^{33,34}. This diverges from the phase predicted by the equilibrium phase diagram, which is the Ni_3Sn_4 IMC¹¹. According to Belyakov and Gourlay^{11,13}, Ni_3Sn_4 has growth advantages



Element	Wt %	At %
SnL	90.80	87.23
FeK	0.50	1.01
NiK	5.01	9.72
PbL	3.69	2.03
Total	100.00	100.00



Element	Wt %	At %
SnL	92.38	85.65
FeK	0.57	1.11
NiK	7.06	13.23
Total	100.00	100.00

Figure 9. Compositions by SEM-EDS of the plate-like intermetallics related to the NiSn₄ eutectic phase in both the eutectic (a) Sn-0.2wt%Ni and the hypereutectic (b) Sn-0.5wt%Ni alloys

over equilibrium Ni₃Sn₄ due to easier interface attachment kinetics with β-Sn during the eutectic growth.

The prevalence of cells under relatively low cooling rates characterized the Sn-0.2wt.%Ni alloy, as stated before. This may be also related to the presence of iron during solidification as noted in the EDS-SEM results (Fig 9 and Fig. 10). This iron content appears to be originated from the interaction between the steel bottom-part mold and the molten alloy. Considerable amounts of iron were found for positions closer to the metal/mold interface, being detected by SEM-EDS until P=10mm. Canté and co-authors³⁵ observed that the addition of 1.0wt.%Fe in the Al-1.0wt.%Ni alloy prevented the growth of dendrites. The ternary Al-1.0wt.%Ni-1.0wt.%Fe alloy was characterized by an arrangement of cells while a dendritic array prevailed for the binary Al-1.0wt.%Ni alloy. It seems that iron (Fe) is able to assist the growth

of cells, as observed in the case of the Sn-0.2wt.%Ni alloy (see Fig. 5), even for fairly low cooling rates.

Low fraction of primary intermetallics in hypereutectic compositions allowed single crystals to be extracted from the matrix by selective etching of the β-Sn phase. The microstructures in the initial positions of the Sn-0.5wt.%Ni alloy casting (P=5mm and P=10mm) refer to tip cooling rates (\dot{T}_L) and tip growth rates (V_L) higher than 16.0K/s and 2.0mm/s respectively. On the other hand, positions farther from the cooled bottom of the casting (P > 30mm) are associated with \dot{T}_L and V_L lower than 3.5K/s and 0.6mm/s respectively.

As can be observed in Fig. 10, the hypereutectic samples contain many (up to three) morphologies of NiSn intermetallics coexisting in the same microstructure. Samples referring to $\dot{T}_L > 16.0$ K/s, as that shown in Fig. 10(a), are characterized by: elongated plate-like, tile-like particles (highlighted in blue); and particles of complex geometry outlined in red. As

verified by the SEM-EDS results either the plate-like (right SEM image in Fig. 10(a)) or the tile-like (left SEM image) particles refer to the Ni_3Sn_4 phase. The number of facets in "tiles" is lower than that observed in the "plates". In addition, the "tiles" are shorter than the "plates".

The Ni_3Sn_4 IMC also grew for samples that experiencing slow cooling rates ($\dot{T}_L < 3.5$ K/s; Fig. 10(b)). Within this nature, the fraction of primary particles was observed to be lower than that characterizing the microstructures of the fast-cooled samples. Shorter sheet-like particles prevailed within these samples. This means that the morphology of the Ni_3Sn_4 IMC changed from longer plates at 16 K/s to shorter sheets at 3.5 K/s.

In a recent study devoted to the formation of intermetallics in Sn-Ni alloys¹¹ it was found that both primary Ni_3Sn_4 and primary NiSn_4 might form for hypereutectic compositions. According to this study, two factors appear to be decisive on which intermetallic will prevail: the cooling rate and the alloy Ni content. In the present investigation, considering

the levels of cooling rate and alloy Ni content, only primary particles growing as Ni_3Sn_4 have been identified.

3.4. Tensile properties and wettability of Sn-Ni alloys

Fig. 11 plots the ultimate tensile strength (σ_u), yield tensile strength (σ_y) and strain to failure (δ) as a function of the microstructural spacings. Hall-Petch type expressions were derived for both alloys and for the three tensile properties, so that a direct comparison is possible. While the strength increases with the decrease in spacing, the ductility shows opposite trends.

The NiSn_4 IMC having a plate-like morphology is considered better distributed between the cells for finer cellular arrangements. Consequently, this explains the improvement in the strength values with the increase in $\lambda_c^{-1/2}$, as observed in Fig. 11(a) and Fig. 11(b). The rigid and interconnected finer eutectic arrangements, as can be seen in Fig. 9 and 10, may boost the strength of the Sn-0.2 and 0.5wt.%Ni alloys.

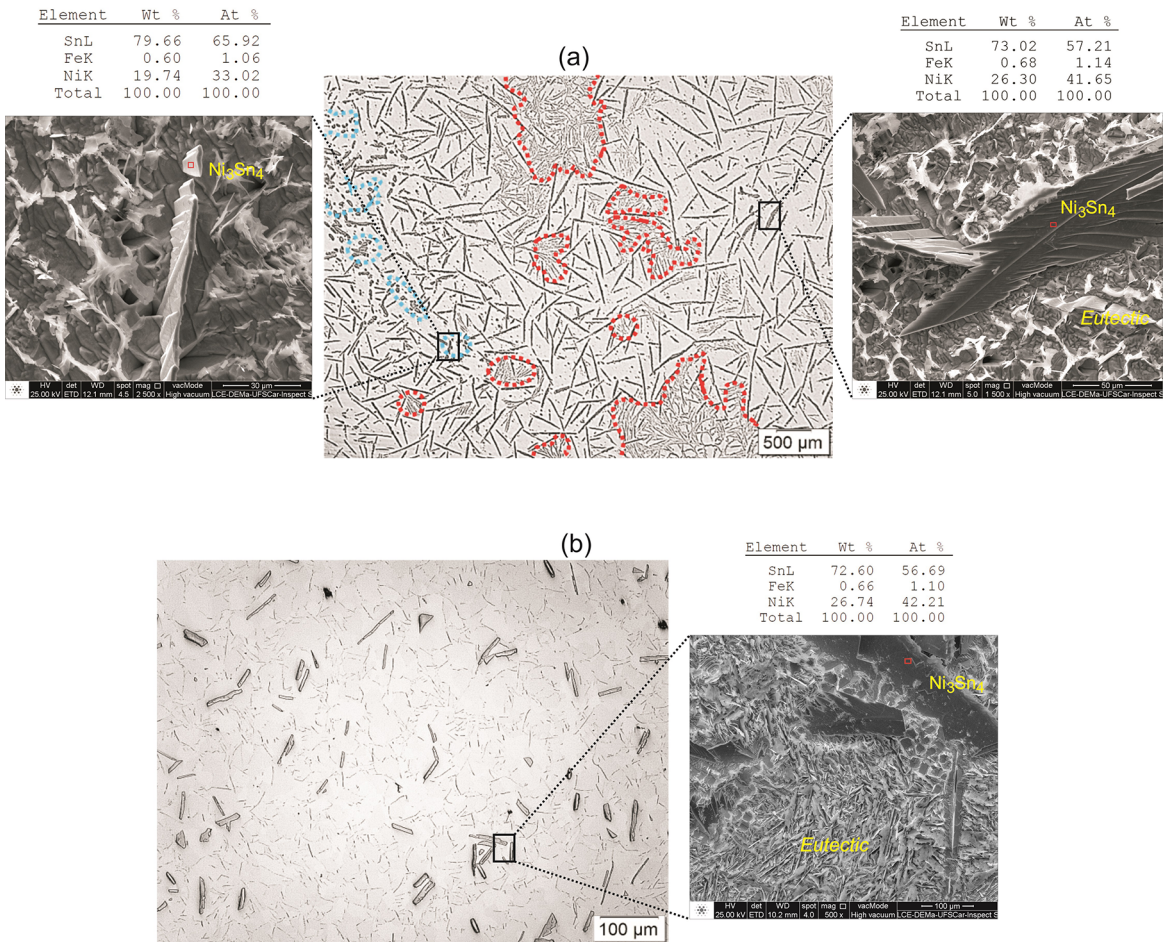


Figure 10. Transverse optical and SEM-EDS microstructures emphasizing the formed Ni_3Sn_4 primary phase along the length of the Sn-0.5wt.%Ni alloy casting: (a) P=5mm and (b) P=40mm, where P is the position from the cooled surface of the alloy casting

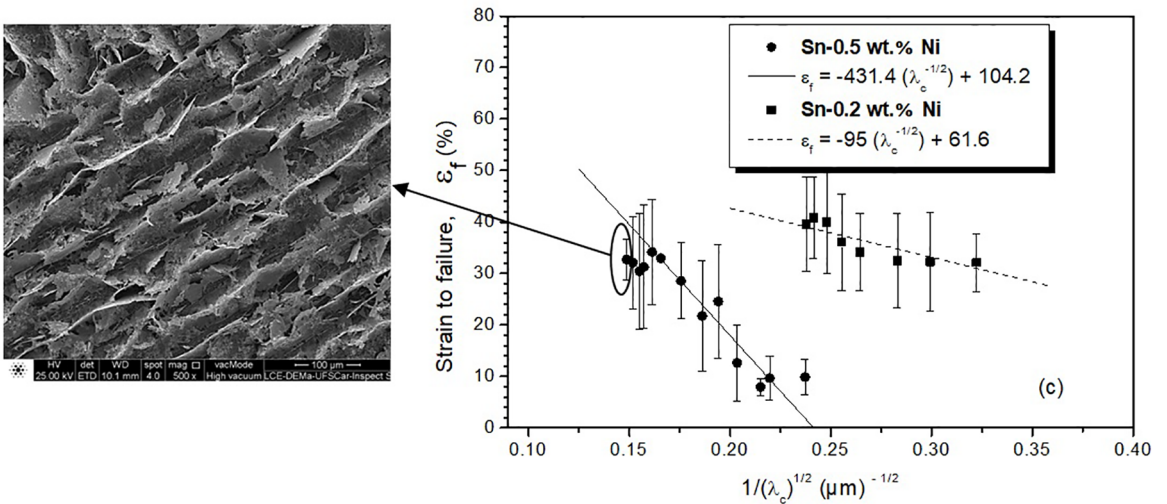
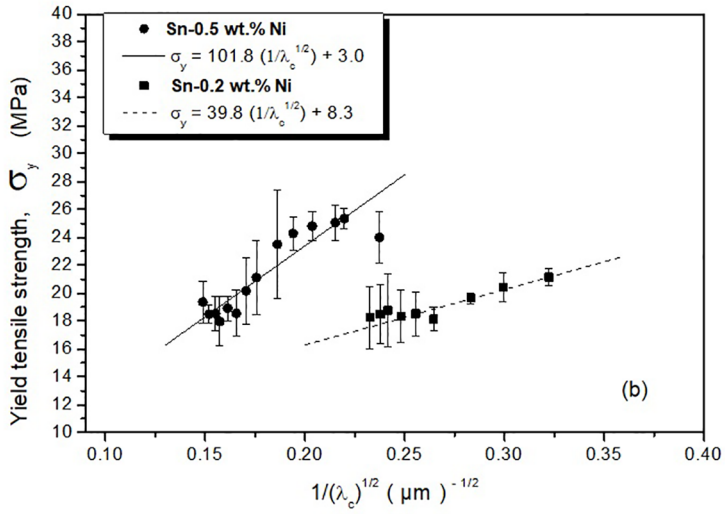
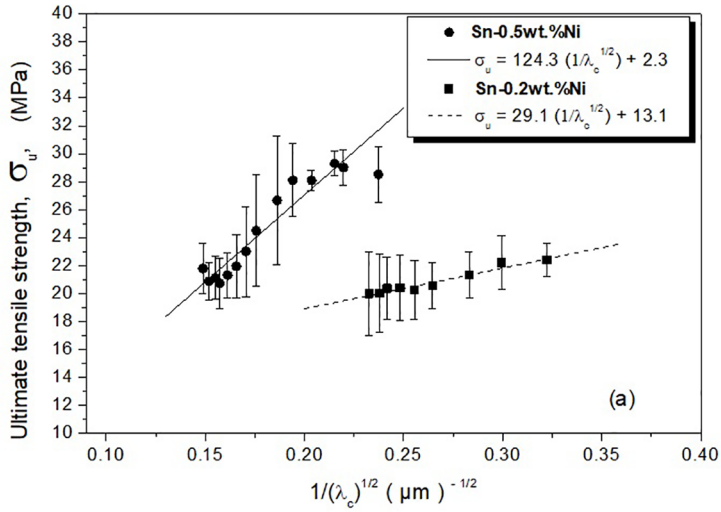


Figure 11. Tensile properties and their correlations with the microstructural spacings for the Sn-0.2 and 0.5 wt.%Ni alloys: (a) Ultimate tensile strength vs. $(\lambda_c)^{-1/2}$; (b) yield tensile strength vs. $(\lambda_c)^{-1/2}$ and (c) strain to failure vs. $(\lambda_c)^{-1/2}$

Due to the growth of hard intermetallics particles, the Sn-0.5wt.%Ni alloy specimens resulted in higher σ_u and σ_y . However, much lower δ is attained as compared to the results found for the eutectic Sn-0.2wt.%Ni alloy.

Even though δ values are generally lower for the hypereutectic alloy, some improvement appears to be achievable for higher λ_c , i.e., for cellular regions in the alloy casting which were grown under slower cooling conditions. The hypereutectic alloy microstructures in these regions consist of Sn-rich plate-like together with regular cells surrounded by the β -Sn+NiSn₄ eutectic structure as can

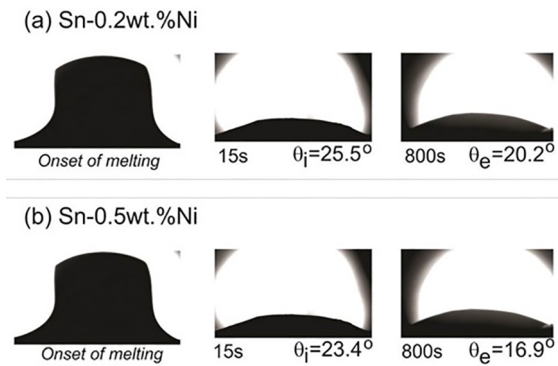


Figure 12. Advancing contact angles of the Sn-Ni droplets on AISI 1020 steel surface showing the initial, θ_i , and equilibrium angles, θ_e , for the (a) Sn-0.2wt.%Ni and (b) Sn-0.5wt.%Ni alloys

be seen in the inserted SEM microstructure in Fig. 11(c). Higher ductility values were attained for such samples.

Two different periods of the experimental wetting scatter are considered during the progressing of contact angles for both examined alloys, which are initial instants (first 45s) referred as initial angles θ_i ; and ending part of the curves when an equilibrium regime is achieved (last 45s). This is related to the equilibrium contact angles, θ_e .

Fig. 12 shows these wetting angles for both Sn-0.2 and 0.5 wt.%Ni alloys. Values of both θ_i and θ_e determined for each alloy are shown in Fig. 12. It is worth noting that the Sn-0.5wt.%Ni alloy presented a slightly higher wettability than that observed for the eutectic alloy. This is because of the lower contact angles measured for the Sn-0.5wt.%Ni alloy.

Although very different amounts of Ni in the examined Sn-Ni alloys may result in variation of alloy properties, such as thermal diffusivity and latent heat of fusion, the lower θ_i observed for the hypereutectic alloy may contribute to explain the higher \dot{T} seen in Fig. 3. Hence, the higher wettability of the Sn-0.5wt.%Ni alloy against the steel substrate may interfere in the evolution of solidification of the alloy, i.e., in \dot{T}_E .

4. Conclusions

- The macrostructures of the DS Sn-0.2wt.%Ni and Sn-0.5wt.%Ni alloys castings were shown to be formed

by vertically aligned columnar grains parallel to the heat flow pathways. A microstructure formed by β -Sn cells surrounded by the metastable β -Sn+NiSn₄ eutectic mixture prevailed for both examined Sn-Ni alloys, despite the presence of the Ni₃Sn₄ primary intermetallics for the Sn-0.5wt.%Ni alloy.

- A reverse cellular/dendritic transition of the eutectic morphology was shown to occur for the Sn-0.2wt.%Ni alloy casting, in which high cooling rate cells prevailed for cooling rates > 1.2 K/s. For the Sn-0.5wt.%Ni alloy casting it was shown that a transition from regular cells to a plate-like cellular microstructure occurs for cooling rates lower than 1.4 K/s.
- Experimental growth laws describing the evolution of cellular spacings with both the cooling rate and the growth rate have been proposed:
Sn-0.2wt.%Ni alloy: $\lambda_c = 22 \dot{T}_E^{-0.55} / \lambda_c = 5.5 V_E^{-1.1}$
Sn-0.5wt.%Ni alloy: $\lambda_c = 35 \dot{T}_E^{-0.55} / \lambda_c = 4 V_E^{-1.1}$
 λ_c [μm]; \dot{T} [$^{\circ}\text{C/s}$] and V_L [mm/s].
- Hall-Petch type correlations relating the ultimate tensile strength (σ_u), yield tensile strength (σ_y) and strain to failure (δ) as a function of the microstructural spacings have been proposed:
Sn-0.2wt.%Ni alloy:
$$\sigma_u = 29.1 (1/\lambda_c^{1/2}) + 13.1 / \sigma_y = 39.8 (1/\lambda_c^{1/2}) + 8.3 / \varepsilon_f = -95 (1/\lambda_c^{1/2}) + 61.6$$

Sn-0.5wt.%Ni alloy:
$$\sigma_u = 124.3(1/\lambda_c^{1/2}) + 2.3 / \sigma_y = 101.8 (1/\lambda_c^{1/2}) + 3.0 / \varepsilon_f = -431.4 (1/\lambda_c^{1/2}) + 104.2$$

 σ [MPa]; ε_f [%] and λ_c [μm]
- The Sn-0.5wt.%Ni alloy was shown to have a slightly higher wettability than that observed for the Sn-0.2wt.%Ni eutectic alloy, that is, initial contact angles θ_i of 23.4° and 25.5°, respectively.

5. Acknowledgements

The authors are grateful for the financial support provided by FAPESP (São Paulo Research Foundation, Brazil: grants 2015/11863-5; 2016/18186-1; 2017/12741-6; 2017/15158-0), CNPq and the Postgraduate Program in Materials Science and Engineering (PPGCEM-UFRN).

6. References

1. El-Rehim AFA, Zahrana HY. Investigation of microstructure and mechanical properties of Sn-xCu solder alloys. *Journal of Alloys and Compounds*. 2017;695:3666-3367.
2. Yang L, Zhang Y, Dai J, Jing Y, Ge J, Zhang N. Microstructure, interfacial IMC and mechanical properties of Sn-0.7Cu-xAl (x = 0-0.075) lead-free solder alloy. *Materials & Design*. 2015;67:209-216.

3. Belyakov SA, Xian JW, Sweatman K, Nishimura T, Akaiwa T, Gourlay CM. Influence of bismuth on the solidification of Sn-0.7Cu-0.05Ni-xBi/Cu joints. *Journal of Alloys and Compounds*. 2017;701:321-334.
4. Byk U, Marasli N. Dependency of eutectic spacings and microhardness on the temperature gradient for directionally solidified Sn-Ag-Cu lead-free solder. *Materials Chemistry and Physics*. 2010;119(3):442-448.
5. Pereira PD, Spinelli JE, Garcia A. Combined effects of Ag content and cooling rate on microstructure and mechanical behavior of Sn-Ag-Cu solders. *Materials & Design*. 2013;45:377-383.
6. Osrio WR, Leiva DR, Peixoto LC, Garcia LR, Garcia A. Mechanical properties of Sn-Ag lead-free solder alloys based on the dendritic array and Ag₃Sn morphology. *Journal of Alloys and Compounds*. 2013;562:194-204.
7. Wang YW, Chang CC, Kao CR. Minimum effective Ni addition to SnAgCu solders for retarding Cu₃Sn growth. *Journal of Alloys and Compounds*. 2009;478(1-2):L1-L4.
8. Nishikawa H, Komatsu A, Takemoto T. Effect of Ni or Co Addition to Sn-Ag Solder on Microstructure and Joint Strength at Interface. *Materials Transaction*. 2008;49(7):1518-1523.
9. Ma H, Suhling JC. A review of mechanical properties of lead-free solders for electronic packaging. *Journal Materials Science*. 2009;44(5):1141-1158.
10. Wu CML, Yu DQ, Law CMT, Wang L. Properties of lead-free solder alloys with rare earth element additions. *Materials Science and Engineering: R. Reports*. 2004;44(1):1-44.
11. Belyakov SA, Gourlay CM. NiSn₄ formation during the solidification of Sn-Ni alloys. *Journal of Alloys and Compounds*. 2012;25:48-59.
12. Xavier MGC, Cruz CB, Kakitani R, Silva BL, Garcia A, Cheung N, et al. Directional solidification of a Sn-0.2Ni solder alloy in water-cooled copper and steel molds: Related effects on the matrix micromorphology, nature of intermetallics and tensile properties. *Journal of Alloys and Compounds*. 2017;723:1039-1052.
13. Belyakov SA, Gourlay CM. Role of Fe impurities in the nucleation of metastable NiSn₄. *Intermetallics*. 2013;37:32-41.
14. Silva BL, Garcia A, Spinelli JE. Complex eutectic growth and Bi precipitation in ternary Sn-Bi-Cu and Sn-Bi-Ag alloys. *Journal of Alloys and Compounds*. 2017;691:600-605.
15. Osrio WR, Peixoto LC, Garcia LR, Mangelinck-Nol N, Garcia A. Microstructure and mechanical properties of Sn-Bi, Sn-Ag and Sn-Zn lead-free solder alloys. *Journal of Alloys and Compounds*. 2013;572:97-106.
16. Gourlay CM, Nogita K, Read J, Dahle AK. Intermetallic Formation and Fluidity in Sn-rich Sn-Cu-Ni Alloys. *Journal of Electronic Materials*. 2010;39(1):56-69.
17. Spinelli JE, Rosa DM, Ferreira IL, Garcia A. Influence of melt convection on dendritic spacings of downward unsteady-state directionally solidified Al-Cu alloys. *Materials Science and Engineering: A*. 2004;383(2):271-282.
18. Donelan P. Modelling microstructural and mechanical properties of ferritic ductile cast iron. *Materials Science and Technology*. 2000;16(3):261-269.
19. Moura ITL, Silva CLM, Cheung N, Goulart PR, Garcia A, Spinelli JE. Cellular to dendritic transition during transient solidification of a eutectic Sn-0.7wt%Cu solder alloy. *Materials Chemistry and Physics*. 2012;132(1):203-209.
20. Felberbaum M, Ventura T, Rappaz M, Dahle AK. Microstructure formation in Sn-Cu-Ni solder alloys. *JOM*. 2011;63:52.
21. Rosa DM, Spinelli JE, Ferreira IL, Garcia A. Cellular growth during transient directional solidification of Pb-Sb alloys. *Journal of Alloys and Compounds*. 2006;422(1-2):227-238.
22. Reinhart G, Gandin CA, Mangelinck-Nol N, Nguyen-Thi H, Spinelli JE, Baruchel J, et al. Influence of natural convection during upward directional solidification: A comparison between in situ X-ray radiography and direct simulation of the grain structure. *Acta Materialia*. 2013;61(13):4765-4777.
23. Silva BL, Cheung N, Garcia A, Spinelli JE. Thermal Parameters, Microstructure, and Mechanical Properties of Directionally Solidified Sn-0.7 wt.%Cu Solder Alloys Containing 0 ppm to 1000 ppm Ni. *Journal of Electronic Materials*. 2013;42(1):179-191.
24. Kong Y, Shao J, Wang W, Liu Q, Chen Z. Electroless Sn-Ni alloy plating with high Sn content free of activation pretreatment. *Journal of Alloys and Compounds*. 2009;477(1-2):328-332.
25. Reyes RV, Bello TS, Kakitani R, Costa TA, Garcia A, Cheung N, et al. Tensile properties and related microstructures aspects of hypereutectic Al-Si alloys directionally solidified under different melt superheats and transient heat flow conditions. *Materials Science and Engineering: A*. 2017;685:235-243.
26. Gndz M, adirli E. Directional solidification of aluminium-copper alloys. *Materials Science and Engineering: A*. 2002;327(2):167-185.
27. McCartney DG, Hunt JD. Measurements of cell and primary dendrite arms spacing in directionally solidified aluminium alloys. *Acta Metallurgica*. 1981;29(11):1851-1863.
28. Okamoto H. *Phase Diagrams of Dilute Binary Alloys*. Materials Park: ASM International; 2002.
29. Kurz W, Fisher DJ. *Fundamentals of Solidification*. Aedermannsdorf: Trans Tech Publications; 1992. p. 85-87.
30. Moreno GR, Silva BL, Bogno AA, Henein H, Spinelli JE. Microstructure-property relations in as-atomized and as-extruded Sn-Cu (-Ag) solder alloys. *Journal of Alloys and Compounds*. 2016;680:259-267.
31. Takemoto T, Takemoto M. Dissolution of stainless steels in molten lead-free solders. *Soldering & Surface Mount Technology*. 2006;18(3):24-30.
32. Xu W, Feng YP, Li Y, Li ZY. Cellular growth of Zn-rich Zn-Ag alloys processed by rapid solidification. *Materials Science and Engineering: A*. 2004;373(1-2):139-145.
33. Schimpf C, Kalanke P, Shang SL, Liu ZK, Leineweber A. Stacking disorder in metastable NiSn₄. *Materials & Design*. 2016;109:324-333.
34. Wang CH, Kuo C, Chen H, Chen S. Effects of current density and temperature on Sn/Ni interfacial reactions under current stressing. *Intermetallics*. 2011;19(1):75-80.
35. Cant MV, Brito C, Spinelli JE, Garcia A. Interrelation of cell spacing, intermetallic compounds and hardness on a directionally solidified Al-1.0Fe-1.0Ni alloy. *Materials & Design*. 2013;51:342-346.